Methods in Oceanography 17 (2016) 319–334

Contents lists available at ScienceDirect

Methods in Oceanography

journal homepage: www.elsevier.com/locate/mio

Full length article

Observations and parameterizations of surfzone albedo

Gregory Sinnett*, Falk Feddersen

Scripps Institution of Oceanography, University of California, San Diego, La Jolla CA 92093, United States

HIGHLIGHTS

- Surfzone albedo can reach 0.45 and varies rapidly with breaking-wave foam.
- Image-based parameterization accurately predicts albedo at wave time scales.
- Wave-model based parameterization predicts time-averaged cross-shore albedo.

ARTICLE INFO

Article history:
Received 15 January 2016
Received in revised form
13 June 2016
Accepted 17 July 2016
Available online 21 August 2016

Keywords:
Surfzone
Albedo
Whitewater
Wave breaking
Parameterization

ABSTRACT

Incident shortwave solar radiation entering the ocean depends on albedo α and plays an important role in the temperature variability and pathogen mortality of the nearshore region. As foam has an elevated albedo, open-ocean albedo parameterizations include whitecapping effects through a wind-based foam fraction. However, surfzone depth-limited wave breaking does not require wind. Surfzone albedo observations are very rare, the variability of surfzone albedo is not known, and parameterizations are not available. New, year-long upwelling and downwelling shortwave radiation observations were made from the Scripps Institution of Oceanography pier spanning the surfzone and inner-shelf. Surfzone albedo was elevated due to foam with mean observed albedo of $\alpha = 0.15$ and one-minute average albedo as high as $\alpha = 0.45$, far exceeding expected albedo (0.06) from standard parameterizations. Using a pier-mounted GoPro camera, an image-based albedo parameterization is developed that estimates the fractional foam area to derive albedo. This parameterization has high skill ($r^2 = 0.90$) on time scales as short as a wave period (9 s). A second wave-model based parameterization for (hourly) averaged albedo is developed relating the non-dimensional roller energy dissipation to the mean

* Correspondence to: 9500 Gilman Drive, La Jolla, CA 92093-0209, United States.
E-mail address: gsinnett@ucsd.edu (G. Sinnett).

http://dx.doi.org/10.1016/j.mio.2016.07.001

foam fraction and thus albedo. The parameterization has good skill ($r^2 = 0.68$) and resolves cross-shore albedo variations. These new parameterizations can be used where imagery is available or wave models are applicable, and can be used to constrain local heat budgets and pathogen mortality.

1. Introduction

The nearshore region ($\leq$ 7 m water depth) is critical both economically and ecologically. The region is a center for tourism, recreation, and commercial use, and is also home to a wide variety of fish, birds, plants and invertebrates. Water temperature is an important ecological aspect, affecting growth rates, recruitment rates, egg-mass production, pathogen ecology and many other factors (e.g., Phillips, 2005; Fischer and Thatje, 2008; Broitman et al., 2005; Goodwin et al., 2012; Halliday, 2012). In this sensitive region, incident shortwave solar radiation entering the ocean (Q_{sw}) plays an important role in both the temperature variability (Sinnett and Feddersen, 2014) and pathogen mortality through UV-B photobiological damage (e.g., Sinton et al., 1994, 2002).

Shortwave solar radiation entering the ocean is defined as

$$Q_{sw} = Q_d - Q_u, \tag{1}$$

where Q_d is the total downwelling (downward) component of solar shortwave radiation, and Q_u is the upwelling (upward) component of shortwave radiation reflected from the ocean surface. The albedo α (surface reflection coefficient) is defined as

$$\alpha = \frac{Q_u}{Q_d}, \tag{2}$$

making

$$Q_{sw} = (1 - \alpha)Q_d. \tag{3}$$

Under direct sun, open ocean albedo α depends on the solar zenith angle θ_s (the angle of sun declination from vertical) and has a daily average of $\alpha \approx 0.06$ (Payne, 1972; Briegleb et al., 1986; Taylor et al., 1996). Under cloudy (diffusely lit) skies, open ocean albedo is near 0.06 and is independent of θ_s (Payne, 1972). However, wind generates ocean whitecaps (foam) (e.g., Monahan, 1971; Monahan and Muircheartaigh, 1980) associated with elevated albedo. Wind also enhances the sea-surface slope variability (e.g., Ross and Dion, 2007), which affects albedo at large solar zenith angles (e.g., Saunders, 1967). Laboratory measurements indicate that pure foam has albedo $\alpha = 0.55$ (Whitlock et al., 1982). For a fractional surface coverage of foam ζ, the combined effects of foam and open water on albedo are often (e.g., Koepke, 1984; Frouin et al., 1996; Jin et al., 2011) represented as

$$\alpha = \zeta\alpha_f + (1 - \zeta)\alpha_\theta, \tag{4}$$

where α_f is the foam albedo, and α_θ is the parameterized solar zenith angle dependent open ocean albedo (e.g., Taylor et al., 1996). The foam fraction ζ from open ocean whitecapping has been parameterized using a surface wind speed $|u_w|$ dependence (e.g., Hansen et al., 1983; Jin et al., 2004, 2011), but has a negligible effect on albedo (less than 0.002) for winds $|u_w| < 12$ m s^{-1} (Payne, 1972; Moore et al., 2000; Frouin et al., 2001).

In the surfzone, foam is generated by depth-limited wave breaking regardless of wind, potentially elevating surfzone α and reducing Q_{sw}. Nearshore temperature evolution (e.g., Sinnett and Feddersen, 2014; Hally-Rosendahl et al., submitted for publication) depends strongly on Q_{sw} in the surfzone and inner-shelf, the region just seaward of the surfzone. Elevated surfzone albedo may also help explain reduced surfzone pathogen mortality relative to the inner-shelf (e.g., Rippy et al., 2013a,b) making the

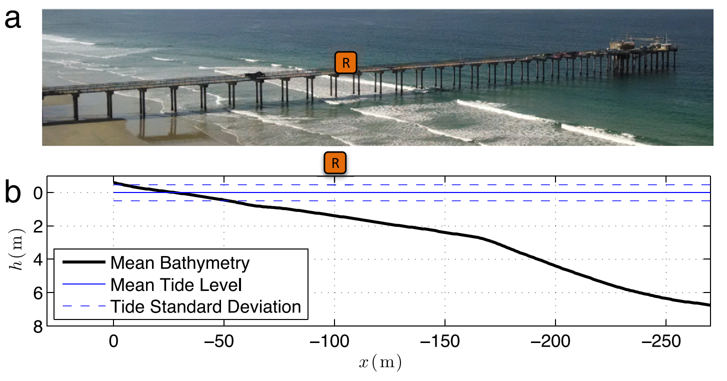

Fig. 1. (a) Photo of the Scripps Institution of Oceanography (SIO) pier (La Jolla, California) and nearshore region at low tide. (b) Mean cross-shore bathymetric profile with mean tide level and approximate tidal extents. The radiometer is located at $x_R = -100$ m (indicated with an orange marker), a location frequently within the surfzone.

surfzone albedo an important factor controlling the ecology of the region. Limited (21 min) surfzone albedo observations at 440–650 nm wavelengths reported elevated albedo up to 0.4–0.6, compared to 0.06 observed in the inner-shelf (Frouin et al., 1996), potentially influencing the surfzone heat budget (Sinnett and Feddersen, 2014). However, no other surfzone albedo observations have been published (to our knowledge) and depth-limited wave-breaking albedo parameterizations do not exist. Thus, the magnitude and variability of surfzone albedo are not known, nor are its impacts on nearshore temperature and pathogen mortality. Making surfzone albedo observations is difficult, thus surfzone albedo parameterizations are needed.

Results from a year-long experiment at the Scripps Institution of Oceanography (SIO) pier measuring nearshore albedo under a wide variety of conditions are presented here, together with tests of two surfzone albedo parameterizations. As surfzone foam is visible in both time-elapsed (e.g., Lippmann and Holman, 1990; Holland et al., 1997; Almar et al., 2010) and snapshot (e.g., Stockdon and Holman, 2000; Chickadel et al., 2003) optical images, the first parameterization uses optical images to estimate foam fraction and albedo. The second parameterization uses a wave and roller transformation model to estimate foam fraction and albedo. The experiment methods and observations are described in Section 2. Results and the two parameterizations are presented in Section 3, discussed in Section 4, and summarized in Section 5.

2. Methods and observations

2.1. Experiment description

Shortwave solar radiation, wave statistics, winds, and water depth were measured between October 25th, 2014 and October 25th, 2015 at the SIO pier (Fig. 1(a)), La Jolla, California (lat 32.867, lon −117.257). Cross-shore (x) bathymetry profiles were made at 0.5 to 1 month intervals (see dots in Fig. 3(a)) between $x = 0$ m (the cross-shore location of the shoreline extents at mean tide at the start of the experiment) and the pier end at $x = -270$ m. NOAA tide gauge station 9410230 at the SIO pier end (in ≈7 m water depth) measured the water level at 6 min intervals. A representative cross-sectional view (Fig. 1(b)) shows the mean bathymetric profile, the Mean Tide Level (MTL) reference height ($h = 0$), and tidal standard deviation (≈0.5 m).

Downwelling, Q_d and upwelling, Q_u shortwave solar radiation was measured by a Campbell Scientific NR01 research grade four-way radiometer (Fig. 2(b)) having two shortwave radiation sensors (wavelengths from 305 nm to 2800 nm) with 2.9 s response time and cosine angle spatial response over a 180° field of view. The sensor noise level is <1.5% of the signal, instrument drift is expected to be <1% per year, and instrument tilt errors are expected to be <2%. Both radiometer sensors were calibrated within one year of their deployment according to ISO 9847.

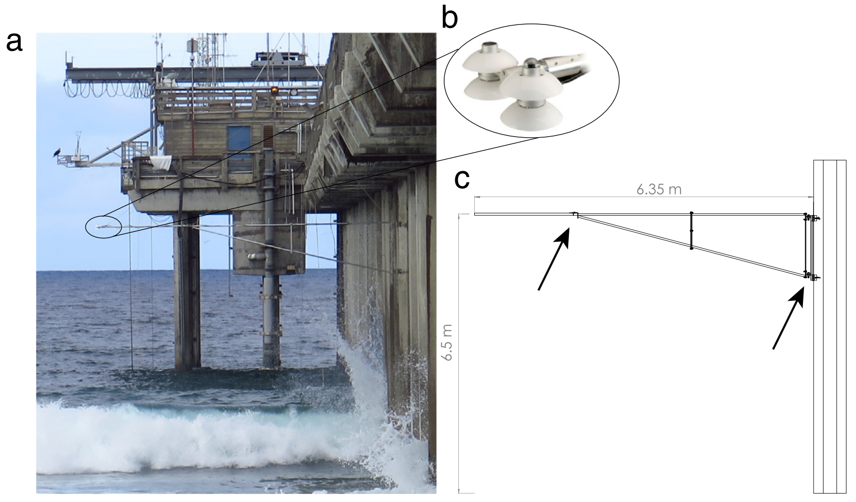

Fig. 2. (a) Photo of the Campbell Scientific NR01 radiometer deployed over the surfzone, mounted on the south side of the SIO pier. (b) A close-up of the NR01 radiometer, consisting of upwelling and downwelling shortwave radiation sensors. (c) A schematic of the boom mount allowing radiometer deployment 6.5 m above MTL at a distance 6.35 m from the pier pilings. Hinges (arrows) allow the boom to pivot laterally and swing vertically for regular radiometer cleaning.

The NR01 radiometer was attached to the end of a custom designed boom arm (Fig. 2(b)) and fitted to the south side of the SIO pier at $x_R = -100$ m. The cross-shore deployment location was chosen so that the radiometer would observe the surfzone roughly two-thirds of the time depending on the tidal depth and wave height. The radiometer was mounted 6.5 m above MTL to avoid significant spray from breaking waves, while assuring that more than 90% of the upwelling signal was confined to a 14 m radius watch circle beneath the instrument. The mounting boom was hinged at the pier end and mid-boom arm (Fig. 2(c) arrows) allowing it to swing parallel and pivot up to the pier deck for cleaning at roughly 5 day intervals.

Generally, the radiometer sampled Q_d and Q_u continuously at 1 Hz, storing the 1 min mean and standard deviation. On 9 days, a GoPro camera with a 72° vertical and 94° horizontal field of view was mounted on the pier deck approximately 2.5 m above the radiometer looking down at the water at ≈45° from horizontal. The camera captured images of the surfzone conditions at two second intervals with a 1/4000 s shutter speed, f/2.8 aperture value and ISO 100 speed rating. During this time the radiometer stored 1 Hz samples directly, allowing image and albedo comparison.

At pier-end, hourly significant wave height $H_s^{(p)}$ and peak period T_p were estimated by the Coastal Data Information Program wave gauge. During times when the wave gauge was offline (July 29 to August 20, 2015) a realtime spectral refraction wave model initialized from offshore buoys (O'Reilly and Guza, 1991, 1998) with very high skill was used. Winds were observed by the NOAA station at the pier end 18 m above MTL and reported as six-minute averaged values. The experiment site latitude and local time were used to calculate solar zenith angle θ_s based on Reda and Andreas (2008).

2.2. Observations

At x_R, the water depth h_R varied due to tidal changes in sea surface elevation and on longer time scales due to bathymetry changes (Fig. 3(a)). Beach profile evolution followed a wintertime (defined here as day 26 on November 20, 2014 to day 126 on February 28, 2015) erosion and summertime (day 212 on May 25, 2015 to day 312 on September 2, 2015) accretion pattern, characteristic of southern California beaches (e.g., Ludka et al., 2015).

Pier-end significant wave height $H_s^{(p)}$ varied between 0.22 m and 2.16 m and peak period T_p between 3 s and 18 s (not shown) with increased wave activity occurring every few days, modulated

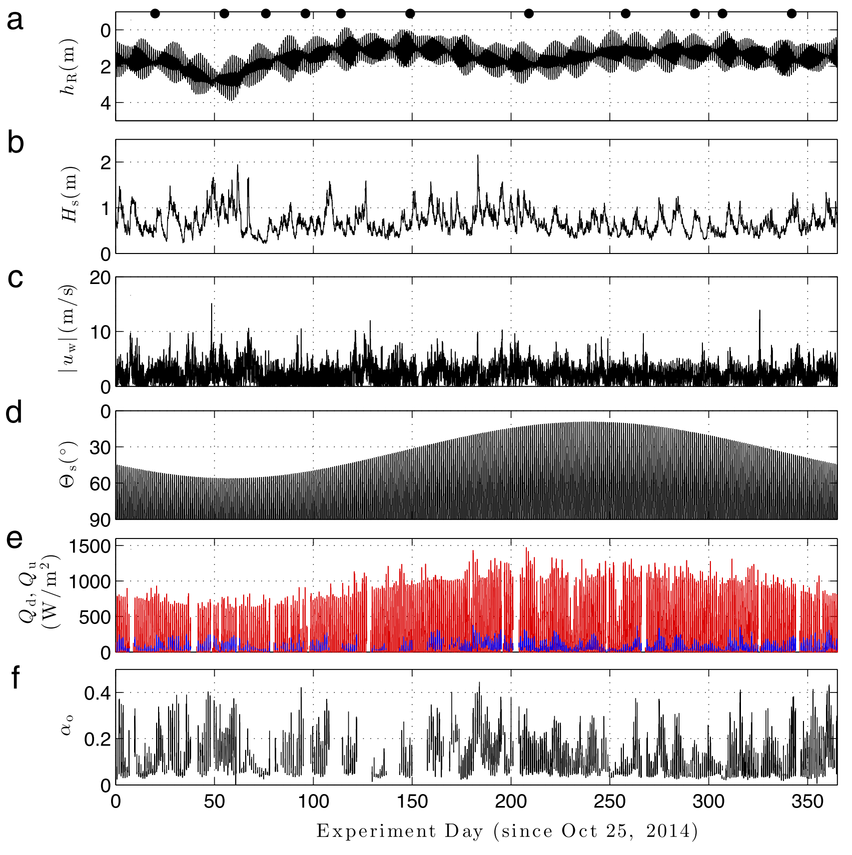

Fig. 3. Hourly time-series over the year-long experimental period of (a) water depth h_R at the radiometer cross-shore location ($x_R = -100$ m), (b) pier-end significant wave height H_s, (c) wind speed $|u_w|$, (d) solar zenith angle θ_s, (e) observed downwelling Q_d (red) and upwelling Q_u (blue) short-wave solar radiation, and (f) observed albedo $\alpha_o = Q_u/Q_d$. Times when Q_d or Q_u were corrupted are removed in (e) and (f). (For interpretation of the references to color in this figure legend, the reader is referred to the web version of this article.)

seasonally with typically stronger wintertime and weaker summertime wave events (Fig. 3b). Winds were typically calm, with average wind speed $|u_w|$ of 2.25 m s^{-1} having diurnal variability and occasional peaks above 10 m s^{-1}, particularly in winter (Fig. 3(c)). Solar zenith angle fluctuated diurnally with daily minimum θ_s varying on an annual time-scale between 56.31° and 9.43° near the winter and summer solstice respectively (Fig. 3(d)).

Foam-free albedo depends on θ_s in direct light (clear sky) but not in diffuse light (cloudy skies) (Payne, 1972). Lighting conditions are characterized with the atmospheric transmittance T_r defined as the ratio of the observed downwelling radiation Q_d to the theoretical maximum Q_d,

$$T_r = \frac{Q_d}{S\cos(\theta_s)\gamma^{-2}}, \tag{5}$$

where S is the solar constant and γ is the ratio of the actual to mean earth–sun separation distance. Direct light conditions are defined when $T_r > 0.6$, and diffuse light conditions are defined when $T_r < 0.3$. The observations were made in 58% clear sky, 16% cloudy sky and 26% mixed sky ($0.3 < T_r < 0.6$) conditions.

Both Q_d and Q_u observations were removed during rain or heavy fog events when the radiometer was affected by moisture. In addition, Q_d and Q_u observations were removed when $\theta_s > 60°$ to avoid nighttime and times when the sun was behind a coastal bluff or very near the horizon. The radiometer was too close to the cross-shore location of exposed sand when, at x_R, the depth $h_R < 1.3$ m (approximately 38% of the time). These observations were also removed. The boom arm extended 6.35 m to the south of the pier to avoid pier shadow under clear skies, when the vast majority of light arrives from the southern sky. However, when the solar azimuth angle $\phi < 109°$ (<0.1% of the time), pier shadows were cast under the radiometer and these observations were removed. In total, ≈50% of daytime data was retained. For pure diffuse light conditions, the true Q_u is slightly underestimated primarily due to pier deck shadow reducing the available downwelling light and also due to pier pilings directly blocking a fraction of the upwelling light from the north. This effect is corrected following Payne (1972) so that the upwelling shortwave radiation is

$$Q_u = Q_{mu}[1 + 0.15(1 - T_r)], \tag{6}$$

where Q_{mu} is the measured upwelling shortwave radiation, T_r is the atmospheric transmittance, and pier geometry sets the coefficient (0.15). This correction has no effect on the results.

Downwelling shortwave radiation Q_d had a predominantly diurnal pattern with seasonal long-term variability and short (<6 h) time-scale variability due to clouds (red in Fig. 3(e)). Clear-sky daily maximum Q_d varied between 610 W m^{-2} in wintertime to 1064 W m^{-2} in the summer. Clouds typically reduced Q_d, but also increased Q_d for short periods (seconds to minutes) due to magnification caused by the "edge-of-cloud" effect (e.g., Davies, 1978; Coakley and Davies, 1986). Reflected shortwave upwelling radiation Q_u (blue in Fig. 3(e)) also varied on diurnal time scales, but contained variability on shorter time scales as well. A time series of over 70,000 one-minute averaged observed albedo observations α_o was generated from the retained Q_d and Q_u with (2). Observed albedo α_o varied from 0.04 to 0.45 on a range of timescales from minutes to many days (Fig. 3(f)).

3. Results

3.1. Albedo dependence on θ_s and waves

Here, the one-minute averaged observed albedo α_o is directly compared to solar zenith angle (θ_s) dependent parameterizations that assume no foam (e.g., Taylor et al., 1996). Observed one-minute averaged albedo α_o are significantly elevated from a solar zenith angle dependent parameterization α_θ (compare dots to red dashed in Fig. 4) for both clear and diffuse light conditions. For $\cos|\theta_s| > 0.5$, α_o varied from near 0.04, typical of α_θ, to 0.45, far exceeding α_θ (Fig. 4). Over all conditions spanning both the surfzone and inner-shelf, the mean albedo was 0.11, nearly twice previous estimates of open-ocean daily averaged albedo (e.g., Payne, 1972). Although the minimum α_o values are consistent with α_θ under both light conditions, the binned mean α_o is roughly one α_o standard deviation higher than α_θ for all θ_s in both clear and diffuse light conditions (compare red diamonds and vertical bars to red dashed curve, Fig. 4).

Depth-limited wave breaking is often well determined by the ratio of local wave height to water depth H_s/h (e.g., Thornton and Guza, 1983). To investigate whether the elevated α_o is due to breaking-wave generated foam or rather due to surface wind speed (as in open ocean parameterizations), the relationship between $\langle\alpha_o\rangle$ (where $\langle\rangle$ denotes an hourly average) and $H_s^{(p)}/h_R$ is examined, where $H_s^{(p)}$ is the pier-end ($x = -270$ m) significant wave height and h_R is the water depth at the radiometer ($x_R = -100$ m). Hourly-averaged $\langle\alpha_o\rangle$ varies between 0.04–0.33 and is strongly related to $H_s^{(p)}/h_R$ (Fig. 5(a)) with $r^2 = 0.64$. Wind speeds at this location were typically weak; mean winds were ≈2 m s^{-1}, and sustained winds over 4 m s^{-1} were observed less than 12% of the time. As expected, winds were not correlated with $\langle\alpha_o\rangle$ (Fig. 5(b)) since total ocean reflectance when winds are less than 8 m s^{-1} is negligible (Koepke, 1984) and whitecapping due to winds below 15 m s^{-1} has not been observed to enhance albedo (Payne, 1972; Frouin et al., 2001). The relationship between $\langle\alpha_o\rangle$ and $H_s^{(p)}/h_R$ demonstrates that for larger incident waves $H_s^{(p)}$ or smaller local water depth h_R, $\langle\alpha_o\rangle$ is elevated in a consistent manner and confirms that the breaking-wave foam strongly contributes to the observed albedo, motivating the following two parameterization approaches.

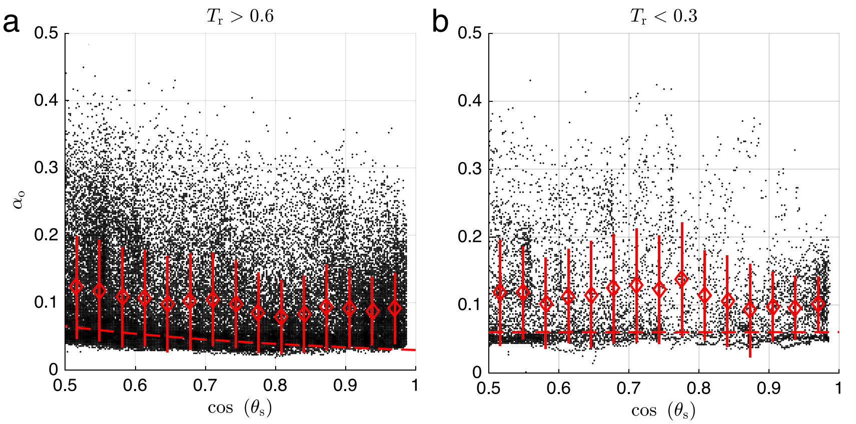

Fig. 4. One-minute averaged observed albedo α_o versus $\cos(\theta_s)$ under (a) clear sky conditions ($T_r > 0.6$) and (b) diffuse light conditions ($T_r < 0.3$). Binned means (red diamonds) and $\pm$ one standard deviation (red vertical lines) of α_o are mostly elevated over the θ_s-only based Taylor et al. (1996) parameterization α_{θ_s} (red dashed). (For interpretation of the references to color in this figure legend, the reader is referred to the web version of this article.)

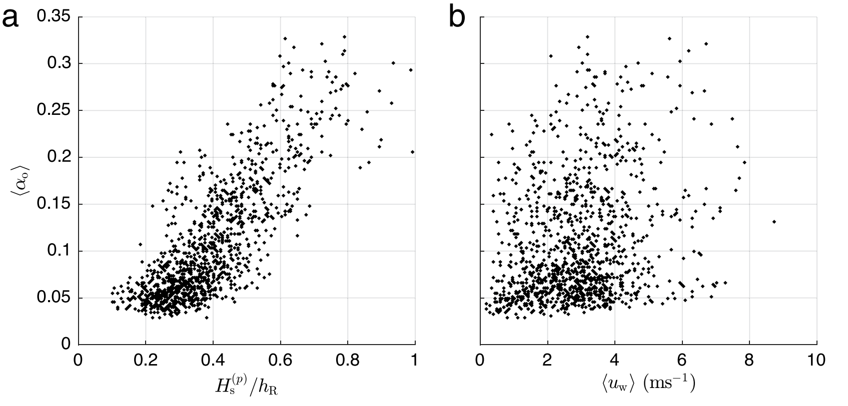

Fig. 5. Hourly averaged observed albedo $\langle \alpha_o \rangle$ versus (a) hourly-observed $H_s^{(p)}/h_R$ where $H_s^{(p)}$ is the significant wave height measured at the pier-end ($x = -270$ m) and h_R is the water depth at the radiometer, and (b) hourly averaged wind speed. Correlation between albedo and wind speed at this site ($r^2 = 0.06$) is not significant from zero at the 95% confidence interval, however albedo is correlated with $H_s^{(p)}/h_R$ ($r^2 = 0.64$).

3.2. Image-based parameterization

Following open-ocean whitecapping parameterizations (e.g., Hansen et al., 1983; Jin et al., 2004, 2011), surfzone albedo is expected to depend on θ_s and the breaking-wave generated foam fraction ζ_W. Time-averaged and snapshot images of the surfzone have successfully been used to identify areas with elevated foam (e.g., Lippmann and Holman, 1990; Stockdon and Holman, 2000). Here, images from the pier-mounted GoPro camera are used to estimate ζ_W and compared to 1-Hz sampled α_o to derive an image-based albedo parameterization.

For a broken wave with extensive foam (Fig. 6(a)), the 1-Hz sampled $\alpha_o = 0.33$, elevated above $\alpha_\theta = 0.06$. In contrast, for foam-free conditions (Fig. 6(b)), $\alpha_o = 0.05$, consistent with expected α_θ. The images were cropped and converted to 0–255 count grayscale G (Fig. 6(c) and (d)) representing the ocean surface light intensity. The grayscale value $G = 0.2989r + 0.5870g + 0.1140b$, where r, b and g are the red, blue and green components respectively, retain luminance while removing hue and saturation. Elevated G can result from foam (white areas in Fig. 6(c)) or sun glint (specular reflection,

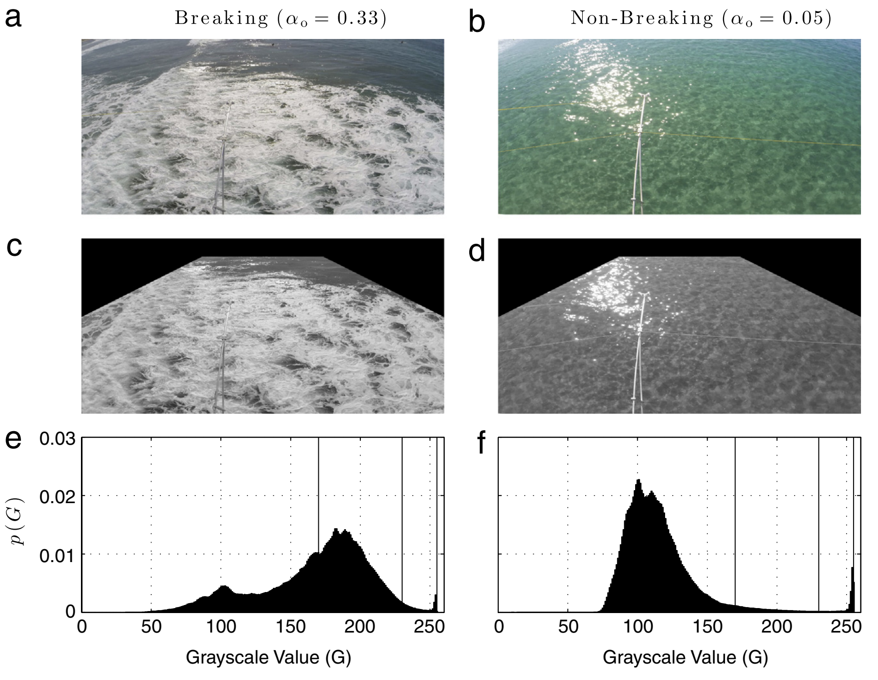

Fig. 6. Images of water below the radiometer (a) during a breaking event when $\alpha_o = 0.33$ and (b) under calm non-breaking conditions when $\alpha_o = 0.05$. Cropped and grayscale converted images of (c) a breaking wave and (d) non-breaking. PDFs of the grayscale values for (e) breaking conditions and (f) non-breaking conditions are delineated (vertical black lines) to show grayscale pixel values classed as "open water" ($G < 170$), "foam" ($170 < G < 230$) and "sun glint" ($G > 230$). The fraction of pixels identified as "foam" (ζ_w) is 0.55 under breaking conditions (left), but only 0.03 for non-breaking conditions (right).

upper left Fig. 6(d)). Typically, sun glint is brighter than foam, which is brighter than foam-free areas, allowing for differentiation between regions using grayscale values.

For the breaking case, the probability density function (PDF) of grayscale pixel values $p(G)$ contains three peaks near 100, 190 and 255 (Fig. 6(e)), corresponding to areas of open water, foam and sun glint in Fig. 6(a). For the non-breaking case, $p(G)$ only has two peaks near 100 and 255 (Fig. 6(d)) corresponding to open water and sun glint. The peak near 190 associated with foam (Fig. 6(c)) is not present. To quantify image area containing open water, foam and sun glint, all grayscale PDFs are first averaged together forming a mean $\overline{p}(G)$ (not shown). Similar to Carini et al. (2015), PDF curvature $\overline{p}''(G)$ maxima define cutoff values between open water, whitewater and sun glint (lines on Fig. 6(e), (f)), here found to be $G = 170$ and $G = 230$. As foam is not a specular reflector (Monahan et al., 1986), sun glint must be from foam free regions and is thus classified as open water. The pixel fraction (as a proxy for surface area) of foam ζ_w is then calculated. For the breaking case (Fig. 6(e)), the pixel fraction attributed to foam was $\zeta_w = 0.55$, and for the non-breaking case (Fig. 6(f)) $\zeta_w = 0.03$. This approach is applied to all images, creating a time series of foam fraction $\zeta_w(t)$ at x_R.

Similar to open ocean whitecapping albedo formulations (4), the image-derived albedo α_I is

$$\alpha_I = \zeta_w \alpha_f + (1 - \zeta_w)\alpha_\theta, \tag{7}$$

where α_θ is the θ_s dependent parameterization for foam-free water, ζ_w is derived from the images, and the foam albedo α_f is considered a free parameter. The 1-Hz α_o varied over 0.02–0.45, spanning a broad range of solar zenith angle ($13.7° < \theta_s < 56°$), depth ($1.3 < h < 2.6$ m) and wave height ($0.45 < H_s < 1.21$ gm) conditions. Minimizing the rms error between α_I and α_o results in a best fit $\alpha_f = 0.465$ and a surfzone albedo parameterization with high skill ($r^2 = 0.90$ with binned-mean $r^2 = 0.97$, Fig. 7).

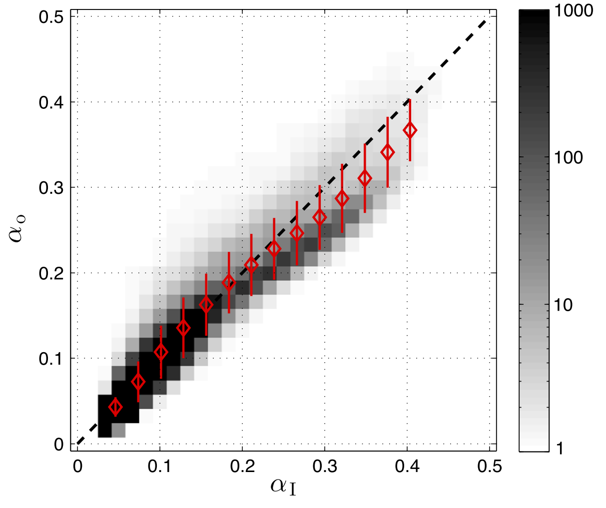

Fig. 7. Gridded logarithmic density (gray scale) of image-derived albedo α_I versus observed albedo α_o sampled at 1 Hz for nine days ($N = 137,547$). The observations were made when θ_s varied between 13.7° and 56°, depth h varied between 1.3 m and 2.6 m, and pier-end H_s varied between 0.45 m and 1.21 m. The best fit $\alpha_f = 0.465$ has fit skill $r^2 = 0.90$ with binned mean (red diamonds) fit skill $r^2 = 0.97$. Binned-mean standard deviations are represented by red lines. Bins contained at least 100 observations. (For interpretation of the references to color in this figure legend, the reader is referred to the web version of this article.)

The high skill of the parameterized α_I is highlighted with a ten-minute example including several breaking wave events from larger wave-groups at 1–2 min intervals (Fig. 8). Breaking waves caused observed albedo α_o (black line, Fig. 8) to increase sharply (in a few seconds), well above α_θ (black dotted). Individual α_o peaks during a large wave-group event (around 200 s) were spaced near $T_p = 9$ s. The highest α_o values, near 0.35, occurred after two or more successive breaking waves almost completely covered the radiometer's field of view. Smaller α_o peaks occurred when breaking events partially filled the field of view or did not break as vigorously. After the initial step-like increase lasting a few seconds, the albedo decayed toward α_θ with time scales $\approx$20 s as the bubbly foam outgassed (e.g., Ma et al., 2011). The asymmetry of the observed albedo α_o rapid increases and slower outgassing decay are well represented by α_I (red curve, Fig. 8), and α_I tracks α_o at both wave group and individual-wave timescales. At α_o peaks (particularly $>$0.2), after a rapid increase, parameterized α_I tends to have a high bias (Fig. 8). This elevated α_I bias for $\alpha_o > 0.2$ is also seen in the scatterplot (Fig. 7) and is discussed further in Section 4. Overall this image-based parameterization predicts the foam-induced elevated α_o unexplained by α_θ (Fig. 4), and the good α_I and α_o time-series agreement (Fig. 8) is also seen at other times and over a wide variety of surfzone conditions.

3.3. *Wave model based albedo parameterization*

Although the image-based parameterization has very high skill, a camera is required, which often is not available. However, given knowledge of one dimensional $h(x)$, wave transformation models have high skill in predicting the cross-shore evolution of wave height (e.g., Ruessink et al., 2001, 2003). This motivates a second albedo parameterization that utilizes a wave model to relate roller dissipation to foam fraction and albedo through (4).

Assuming normally-incident narrow-banded waves on alongshore uniform beaches, one-dimensional wave and roller transformation models (e.g., Thornton and Guza, 1983; Battjes and Stive, 1985; Ruessink et al., 2001) relate wave energy flux gradient to wave-energy dissipation,

$$\frac{d}{dx}(EC_g) = -\langle \epsilon_b \rangle, \tag{8}$$

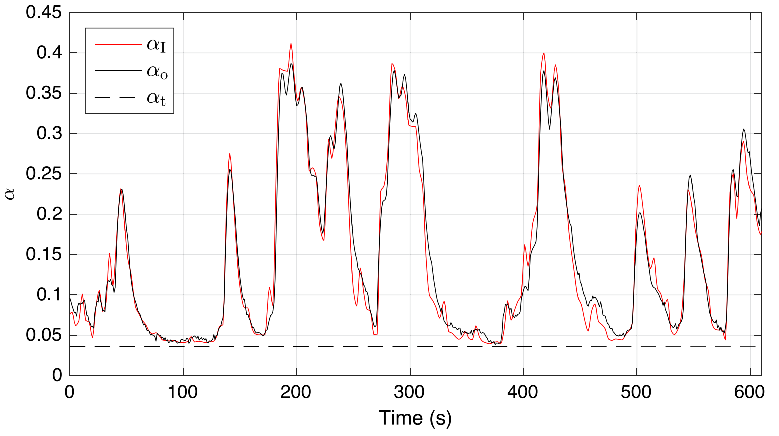

Fig. 8. Ten-minute time series of image-derived albedo α_I (red), observed albedo α_o (black) and parameterized open ocean albedo α_θ (dashed) beginning near noon on September 11, 2015. Water depth $h(x_R) = 1.5$ m with moderate waves ($H_s = 0.6$ m and $T_p = 9$ s at the pier-end) and light winds ($|u_w| = 3.7$ m s^{-1}) with $\theta_s = 31°$. (For interpretation of the references to color in this figure legend, the reader is referred to the web version of this article.)

where E is the wave energy density, C_g is the group velocity given by linear theory, and $\langle \epsilon_b \rangle$ is the bulk breaking wave dissipation. The wave energy density is $E = 1/16\rho g H_s^2$ where ρ is water density, g is gravity and H_s is the local significant wave height. The breaking wave dissipation $\langle \epsilon_b \rangle$ is given by Church and Thornton (1993) with standard breaking parameters ($B = 0.9$ and $\gamma = 0.57$). The roller energy equation is (e.g., Ruessink et al., 2001)

$$\frac{d}{dx}(2E_r c) = -\langle \epsilon_r \rangle + \langle \epsilon_b \rangle, \tag{9}$$

where E_r is the roller energy density and c is the linear theory phase speed. Roller dissipation is defined as (Deigaard, 1993)

$$\langle \epsilon_r \rangle = \frac{2gE_r \sin\beta}{c} \tag{10}$$

with slope $\beta = 0.1$ (e.g., Walstra et al., 1996). The coupled Eqs. (8) and (9) are solved with the specified $h(x)$ and offshore (pier-end) boundary conditions of observed H_s and T_p, with $E_r = 0$.

Example output from the wave and roller model characterizes the cross-shore evolution of H_s (Fig. 9(a)) due to the bathymetric profile (Fig. 9(e)). As waves shoal onshore, wave height increases to $H_s = 1.5$ m at $x = -170$ m where breaking occurs, roller dissipation becomes non-zero (Fig. 9(b)) and wave height decreases. The terraced, non-monotonic bathymetry create undulating regions of elevated $\langle \epsilon_r \rangle$ (e.g., near $x = 140$ m, $x = 90$ m, Fig. 9(b)) and weaker $\langle \epsilon_r \rangle$ (e.g., near $x = 125$ m and $x = 65$ m).

To develop a wave-model based albedo parameterization α_w, the average foam fraction $\langle \zeta_w \rangle$ is hypothesized to depend linearly on non-dimensional ($\widehat{\ }$) wave roller dissipation $\langle \widehat{\epsilon_r} \rangle$ as

$$\langle \zeta_w \rangle = m \langle \widehat{\epsilon_r} \rangle, \tag{11}$$

where $\langle \widehat{\epsilon_r} \rangle$ is non-dimensionalized by wave-dissipation scaling (e.g., Battjes, 1975; Feddersen and Trowbridge, 2005; Feddersen, 2012a,b) as

$$\langle \widehat{\epsilon_r} \rangle = \frac{\langle \epsilon_r \rangle}{\rho (gh)^{3/2}}, \tag{12}$$

and m is a fit parameter found by minimizing rms error between α_o and α_w. The hourly averaged wave-model based albedo is found from (4) using $\langle \zeta_w \rangle$ and $\alpha_f = 0.465$ as in Section 3.2. The radiometer observed α_o is a cosine angle weighted area-average with $\approx$ 14 m radius. To compare the observed

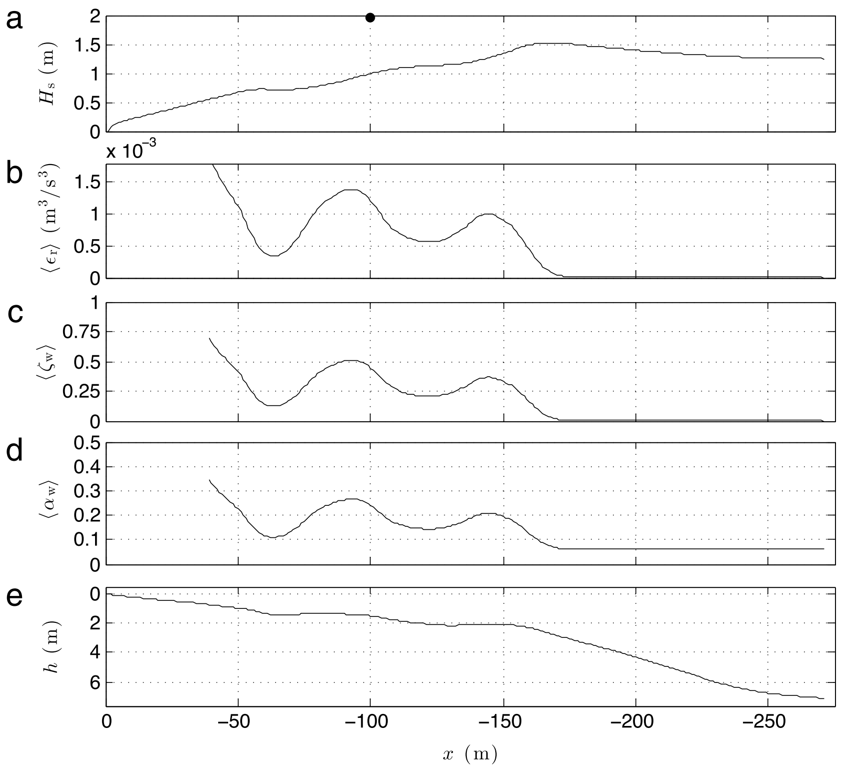

Fig. 9. (a) Modeled significant wave height H_s, (b) modeled wave-roller dissipation $\langle \epsilon_r \rangle$, (c) inferred mean foam fraction $\langle \zeta_w \rangle$, (d) wave-model parameterized albedo $\langle \alpha_w \rangle$, and (e) bathymetry profile $h(x)$ versus cross-shore coordinate x for noon on February 8, 2015. The black dot indicates the radiometer cross-shore location (x_R), which measured $\langle \alpha_o \rangle = 0.27$ under clear skies ($T > 0.6$) while $\theta_s \approx 48°$ at this time. The wave model was initialized with one-hour averaged $H_s = 1.3$ m and $T_p = 13.4$ s measured at the pier-end (assuming incident waves). Modeled quantities are not shown for $h < 0.5$ m.

albedo with the parameterized albedo, $\langle \zeta_w \rangle$ is also area-averaged with an identical cosine weighted response centered at x_R. The resulting foam fraction $\overline{\langle \zeta_w \rangle}$ is both time and area averaged (where $\overline{}$ denotes an area average) and the resulting time and area averaged wave-model based albedo $\overline{\langle \alpha_w \rangle}$ is found from (4).

When the radiometer sampled the surfzone (at x_R, $H_s/h \geq 0.57$), the mean observed surfzone albedo α_o was 0.15, over twice the daily average open ocean albedo parameterization of 0.06. The observed hourly averaged albedo $\langle \alpha_o \rangle$ varied between 0.04 and 0.33, greater than the open ocean albedo parameterization more than 80% of the time. The parameterized $\overline{\langle \alpha_w \rangle}$ was a good predictor of $\langle \alpha_o \rangle$ with significant skill ($r^2 = 0.68$) when best fit parameter $m = 398$ (dots in Fig. 10). The parameterized binned mean $\overline{\langle \alpha_w \rangle}$ (red diamonds in Fig. 10) has high skill ($r^2 = 0.94$) over these widely ranging and elevated albedo conditions. Factors contributing to variance in the binned quantities are discussed in Section 4.

Although $\overline{\langle \alpha_w \rangle}$ is generated from hourly-averaged wave statistics, $\overline{\langle \alpha_w \rangle}$ is able to track albedo changes on time scales related to θ_s, h and H_s (Fig. 11). For example, over six days, the combined effects of θ_s and wave energy at x_R cause the daily average of both $\langle \alpha_o \rangle$ and $\overline{\langle \alpha_w \rangle}$ to vary between 0.06 and 0.18. Albedo also varied by 0.16 in only 4 h on day 2 associated with changes in H_s/h, yet there is still good agreement between $\overline{\langle \alpha_w \rangle}$ and $\langle \alpha_o \rangle$. Albedo estimation at specific cross-shore locations is also possible. The parameterized cross-shore foam fraction $\langle \zeta_w \rangle$ varies from zero offshore to local maxima of $\langle \zeta_w \rangle = 0.3$ and $\langle \zeta_w \rangle = 0.5$ at $x = -140$ m and $x = -90$ m, respectively (Fig. 9(c)), consistent with the range of image inferred ζ_w. The resulting $\langle \alpha_w \rangle(x)$ (Fig. 9(d)) is frequently above the θ_s dependent parameterization at this time ($\alpha_\theta = 0.06$) which is only valid in locations where there is no breaking.

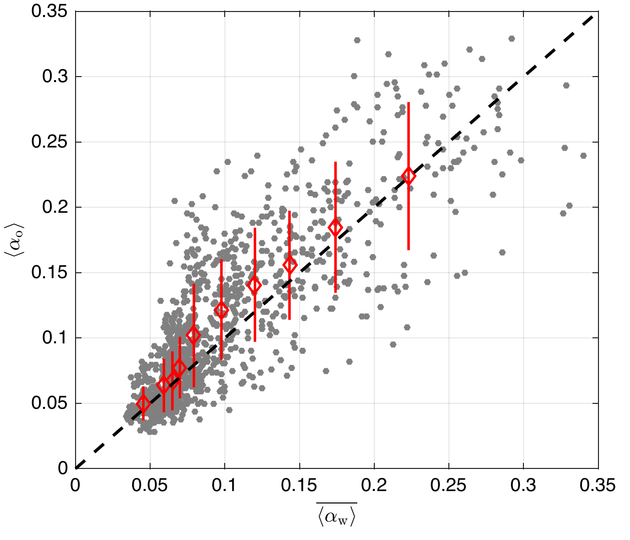

Fig. 10. Hourly-averaged observed albedo $\langle\alpha_o\rangle$ versus the wave-model albedo parameterization $\overline{\langle\alpha_w\rangle}$ ($N = 1169$). The 1:1 line (dotted) is shown with binned means (red diamonds) and $\pm$ standard deviation (red lines). The best fit slope $m = 398$ and skill $r^2 = 0.68$ (binned-mean $r^2 = 0.94$). (For interpretation of the references to color in this figure legend, the reader is referred to the web version of this article.)

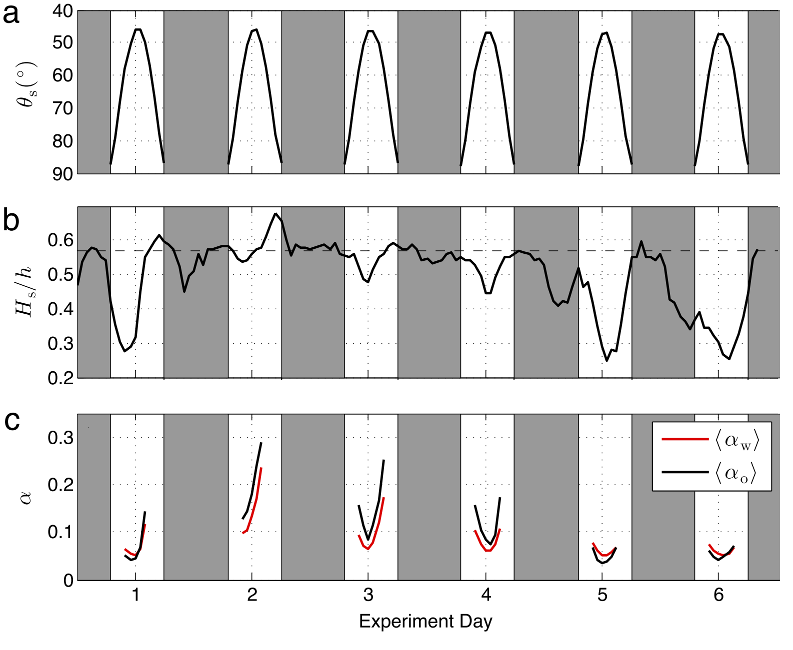

Fig. 11. Six day time series (October 25–30, 2014) of (a) solar zenith angle θ_s, (b) depth normalized significant wave height H_s/h at x_R with expected threshold of significant wave breaking (dotted) (c) observed albedo $\langle\alpha_o\rangle$ (black) and wave parameterized albedo $\langle\alpha_w\rangle$ (red). Nighttime ($\theta_s > 90$) is shaded. (For interpretation of the references to color in this figure legend, the reader is referred to the web version of this article.)

Surfzone albedo can also be parameterized with non-dimensionalized roller-energy instead of roller dissipation, with similar skill.

4. Discussion

Elevated surfzone albedo can impact heat budgets (Sinnett and Feddersen, 2014) and pathogen mortality (e.g., Sinton et al., 2002). Water-entering short-wave solar radiation Q_{sw} is the largest surfzone heat budget term (Sinnett and Feddersen, 2014). An average surfzone albedo increase from $\alpha = 0.06$ to (as observed) $\alpha = 0.15$ would reduce Q_{sw} so that cross-shore advection or wave heating are relatively more important. For example, Sinnett and Feddersen (2014) found a residual surfzone heat export of 5.2×10^3 W m^{-1}. Revising the heat budget using $\alpha = 0.15$, reduces the residual heat export by 30%. Dye tracer can linger in the surfzone for >12 h (Hally-Rosendahl et al., submitted for publication), indicating the time-scales pathogens can remain in bathing waters. Increasing albedo from 0.06 to 0.15 roughly doubles fecal coliform bacterial survival rates (Sinton et al., 2002), increasing potential human health risk if not appropriately accounted for.

The observed albedo α_o is a space and time-average over the radiometer's 14-m radius cosine response and 2.9 s time constant. With propagating breaking waves which continuously outgas bubbles, the radiometer will never instantaneously sample pure foam over its entire field of view. This may explain why the best-fit foam albedo $\alpha_f = 0.465$ is less than the laboratory observed maximum value of 0.55 (Whitlock et al., 1982). Although the image-based α_I predicts α_o with high skill (Fig. 7), for $\alpha_o > 0.2$, α_I is biased high particularly when a breaking wave front passes and $d\alpha/dt$ is large (Fig. 8). The 2.9 s radiometer response time, relative to the near-instantaneous camera response time, may explain this bias at times of step function-like changes in albedo.

The specific grayscale PDF cutoff limits for open water, foam, and sun glint, derived from $\overline{p}''(G)$ extrema, are the result of the lighting and fixed camera settings at this location. To apply this parameterization with another camera or at another location, one must first establish the relevant $\overline{p}''(G)$ based cutoff limits. This method can also be applied to time-averaged images. Good agreement between α_I and α_o was found with a constant foam albedo α_f applied to grayscale values within the foam cutoff limits. The fit may be improved if α_f is a function of G. Furthermore, images were not georectified. The images were cropped to limit the field of view to a relatively small area beneath the radiometer, and the 45° camera angle caused the imaged pixel area to have a similar spatial response as the radiometer. For example, the pixels near the top of the image cover roughly 35% more area than the pixels near the bottom, and the radiometer cosine response reduces the signal by roughly 40% near the top of the image. As the camera and radiometer were sampling with similar spatial weights, image rectification was not needed. However, image rectification may be required if this parameterization technique is applied to images covering a wider area (e.g., ARGUS), or to images taken at shallower angles.

When breaking occurs, $\langle \alpha_o \rangle$ is elevated above α_θ (Figs. 3 and 4), and the wave-model based parameterization has good skill ($r^2 = 0.68$) in predicting α_o (Fig. 10), although significant unexplained variance remains. Waves were assumed to be normally-incident (as expected for long-period waves in $h < 6$ m), and standard wave and roller model coefficients were used. The bathymetry near piers is often scoured (Elgar et al., 2001), which may result in pier-based bathymetry measurement errors. Depth h errors and wave model errors would induce roller energy dissipation $\langle \epsilon_r \rangle$ errors, and eventually $\langle \alpha_w \rangle$ errors, potentially contributing to the unexplained variance in Fig. 10.

5. Summary

Breaking-wave induced foam elevates albedo α relative to foam-free ocean. Open-ocean albedo parameterizations account for foam through a wind speed dependent whitecapping foam fraction ζ_w. However, surfzone depth-limited wave breaking does not depend on wind, and wind-based foam fraction parameterizations are inaccurate in the surfzone. Measuring albedo in the energetic surfzone environment is difficult, and observations of surfzone albedo are very rare. The variability of surfzone albedo is not known, and parameterizations have not been available. Ocean-entering shortwave solar radiation Q_{sw} depends on albedo and affects both temperature variability and pathogen mortality. This motivates new observations of surfzone albedo and the development of two surfzone albedo parameterizations based on camera images and a wave model.

A year-long experiment at the Scripps Institution of Oceanography pier observed upwelling Q_u and downwelling Q_d shortwave radiation spanning the surfzone and inner-shelf over a range of wave and depth conditions. A two-way radiometer was mounted 6.5 m above the mean ocean surface and 6.35 m away from the pier, limiting pier shadow effects. Additional wave, wind, tidal and bathymetric observations were collected. On nine days, a downward-looking GoPro camera fixed above the radiometer location continuously captured water surface images. For solar zenith angle $\theta_s < 60^\circ$, one-minute averaged observed albedo (as large as $\alpha_o = 0.45$) far exceeded the open ocean solar zenith angle parameterized albedo of 0.06. The elevated observed albedo was related to breaking wave conditions under the radiometer and observed albedo was not related to the wind speed.

A surfzone albedo parameterization is developed using images to estimate foam fraction ζ_w, identified by the distribution of grayscale pixels values. This image-based parameterization has high skill ($r^2 = 0.90$), with a best-fit parameter for foam albedo of $\alpha_f = 0.465$, slightly less than laboratory maximum of 0.55 likely due to radiometer finite time and spatial response. This parameterization captures albedo variability on the time-scales of individual waves (9 s) and wave groups (minutes).

A wave-model based parameterization relates non-dimensionalized wave roller energy dissipation to the hourly-averaged foam fraction $\langle \zeta_w \rangle$ and, thus, to albedo. The wave model is initiated with bathymetry and incident wave conditions. This parameterization predicts hourly averaged observations from the radiometer, has good skill ($r^2 = 0.68$), and can resolve cross-shore albedo variations. Bathymetry or wave model errors may contribute to unexplained variance. These new parameterizations are applicable where imagery (e.g., ARGUS) or nearshore wave models are available, and can be used to constrain local heat budgets and pathogen mortality estimation.

Acknowledgments

This work was supported in part by ONR (N00014-15-1-2117) and NSF (OCE-1558695). Gregory Sinnett was supported by a NSF GK12 fellowship (DGE-0841407) and the SIO graduate department. Radiometer boom arm was developed and deployed by B. Woodward, B. Boyd, K. Smith, and R. Grenzeback. Deployment and recovery above difficult surfzone conditions was aided by C. McDonald, R. Walsh, S. Mumma, G. Boyd, L. Parry and the San Diego lifeguards. G. Castelao helped maintain the radiometer during deployment. Wave data was provided by the Coastal Data Information Program (CDIP) with special assistance from W. O'Reilly and C. Olfe. Wind and tidal data was gathered from NOAA station 9410230. Two anonymous reviewers significantly improved this manuscript. We would like to sincerely thank these people and organizations.

References

Almar, R., Castelle, B., Ruessink, B., Sénéchal, N., Bonneton, P., Marieu, V., 2010. Two- and three-dimensional double-sandbar system behaviour under intense wave forcing and a meso–macro tidal range. Cont. Shelf Res. 30 (7), 781–792. http://dx.doi.org/10.1016/j.csr.2010.02.001.

Battjes, J., 1975. Modeling of turbulence in the surfzone. In: Proc. Symposium Modeling Techniques. ASCE, pp. 1050–1061.

Battjes, J.A., Stive, M.J.F., 1985. Calibration and verification of a dissipation model for random breaking waves. J. Geophys. Res. Oceans 90 (C5), 9159–9167. http://dx.doi.org/10.1029/JC090iC05p09159.

Briegleb, B., Minnis, P., Ramanathan, V., Harrison, E., 1986. Comparison of regional clear-sky albedos inferred from satelliete observations and model computations. J. Clim. Appl. Meteorol. 25, 214–226.

Broitman, B., Blanchette, C., Gaines, S., 2005. Recruitment of intertidal invertebrates and oceanographic variability at Santa Cruz Island, California. Limnol. Oceanogr. 50 (5), 1473–1479.

Carini, R.J., Chickadel, C.C., Jessup, A.T., Thomson, J., 2015. Estimating wave energy dissipation in the surf zone using thermal infrared imagery. J. Geophys. Res. Oceans 120 (6), 3937–3957. http://dx.doi.org/10.1002/2014JC010561.

Chickadel, C.C., Holman, R.A., Freilich, M.H., 2003. An optical technique for the measurement of longshore currents. J. Geophys. Res. 108 (C11), 3364. http://dx.doi.org/10.1029/2003JC001774.

Church, J., Thornton, E., 1993. Effects of breaking wave-induced turbulence within a longshore-current model. Coastal Eng. 20 (1–2), 1–28.

Coakley, J.A., Davies, R., 1986. The effect of cloud sides on reflected solar radiation as deduced from satellite observations. J. Atmos. Sci. 43 (10), 1025–1035. 10.1175/1520-0469(1986)043<1025:TEOCSO>2.0.CO2.

Davies, R., 1978. The effect of finite geometry on the three-dimensional transfer of solar irradiance in clouds. J. Atmos. Sci. 35 (9), 1712–1725. 10.1175/1520-0469(1978)035<1712:TEOFGO>2.0.CO2.

Deigaard, R., 1993. A note on the three dimensional shear stress distribution in a surfzone. Coast. Eng. 20, 157–171.

Elgar, S., Guza, R.T., O'Reilly, W.C., Raubenheimer, B., Herbers, T.H.C., 2001. Wave energy and direction observed near a pier. J. Waterw. Port Coastal Ocean Eng. 127, 2–6.

Feddersen, F., 2012a. Scaling surfzone dissipation. Geophys. Res. Lett. 39, L18613.

Feddersen, F., 2012b. Observations of the surfzone turbulent dissipation rate. J. Phys. Oceanogr. 42, 386–399. http://dx.doi.org/10.1175/JPO-D-11-082.1.

Feddersen, F., Trowbridge, J.H., 2005. The effect of wave breaking on surf-zone turbulence and alongshore currents: a modelling study. J. Phys. Oceanogr. 35, 2187–2204.

Fischer, S., Thatje, S., 2008. Temperature-induced oviposition in the brachyuran crab Cancer setosus along a latitudinal cline: Aquaria experiments and analysis of field-data. J. Exp. Mar. Biol. Ecol. 357 (2), 157–164. http://dx.doi.org/10.1016/j.jembe.2008.01.007.

Frouin, R., Iacobellis, S.F., Deschamps, P.-Y., 2001. Influence of oceanic whitecaps on the global radiation budget. Geophys. Res. Lett. 28 (8), 1523–1526. http://dx.doi.org/10.1029/2000GL012657.

Frouin, R., Schwindling, M., Deschamps, P.-Y., 1996. Spectral reflectance of sea foam in the visible and near-infrared: In situ measurements and remote sensing implications. J. Geophys. Res. 101 (C6), 14,361–14,371. http://dx.doi.org/10.1029/96JC00629.

Goodwin, K.D., McNay, M., Cao, Y., Ebentier, D., Madison, M., Griffith, J.F., 2012. A multi-beach study of Staphylococcus aureus, MRSA, and enterococci in seawater and beach sand. Water Res. 46 (13), 4195–4207. http://dx.doi.org/10.1016/j.watres.2012.04.001.

Halliday, E.E.A., 2012. Sands and environmental conditions impact the abundance and persistence of the fecal indicator bacteria enterococcus at recreational beaches (Ph.D. thesis), Massachusetts Institute of Technology.

Hally-Rosendahl, K., Feddersen, F., Guza, R.T., 2014. Cross-shore tracer exchange between the surfzone and the inner-shelf. J. Geophys. Res. submitted for publication.

Hansen, J., Russell, G., Rind, D., Stone, P., Lacis, A., Lebedeff, S., Ruedy, R., Travis, L., 1983. Efficient three-dimensional global models for climate studies: Models i and ii. Mon. Weather Rev. 111, 609–662.

Holland, K., Holman, R., Lippmann, T., Stanley, J., Plant, N., 1997. Practical use of video imagery in nearshore oceanographic field studies. IEEE J. Ocean. Eng. 22 (1), 81–92. http://dx.doi.org/10.1109/48.557542.

Jin, Z., Charlock, T., Smith, W., Rutledge, K., 2004. A parameterization of ocean surface albedo. Geophys. Res. Lett. 31 (22), http://dx.doi.org/10.1029/2004GL021180.

Jin, Z., Qiao, Y., Wang, Y., Fang, Y., Yi, W., 2011. A new parameterization of spectral and broadband ocean surface albedo. Opt. Express 19 (27).

Koepke, P., 1984. Effective reflectance of oceanic whitecaps. Appl. Opt. 23 (11).

Lippmann, T., Holman, R., 1990. The spatial and temporal variability of sand-bar morphology. J. Geophys. Res. 95 (C7), 11,575–11,590. http://dx.doi.org/10.1029/JC095iC07p11575.

Ludka, B.C., Guza, R.T., O'Reilly, W.C., Yates, M.L., 2015. Field evidence of beach profile evolution toward equilibrium. J. Geophys. Res., Oceans 120.

Ma, G., Shi, F., Kirby, J.T., 2011. A polydisperse two-fluid model for surf zone bubble simulation. J. Geophys. Res. 116, c05010. http://dx.doi.org/10.1029/2010JC006667.

Monahan, E.C., 1971. Oceanic whitecaps. J. Phys. Oceanogr. 1 (2), 139–144. http://dx.doi.org/10.1175/1520-0485(1971)001<0139:OW>2.0.CO2.

Monahan, E.C., Muircheartaigh, I., 1980. Optimal power-law description of oceanic whitecap coverage dependence on wind speed. J. Phys. Oceanogr. 10 (12), 2094–2099. http://dx.doi.org/10.1175/1520-0485(1980)010<2094:OPLDOO>2.0.CO2.

Monahan, E., Niocaill, G., Koepke, P., 1986. Oceanographic Sciences Library, Vol. 2. Springer, Netherlands, pp. 251–260. http://dx.doi.org/10.1007/978-94-009-4668-2_23.

Moore, K.D., Voss, K.J., Gordon, H.R., 2000. Spectral reflectance of whitecaps: their contribution to water-leaving radiance. J. Geophys. Res. Oceans 105 (C3), 6493–6499. http://dx.doi.org/10.1029/1999JC900334.

O'Reilly, W., Guza, R., 1991. Comparison of spectral refraction and refraction-diffraction wave models. J. Waterw. Port Coast. Ocean Eng.-ASCE 117 (3), 199–215.

O'Reilly, W., Guza, R., 1998. Assimilating coastal wave observations in regional swell predictions. Part I: Inverse methods. J. Phys. Oceanogr. 28 (4), 679–691.

Payne, R.E., 1972. Albedo of the sea surface. J. Atmos. Sci. 29, 959–970.

Phillips, N., 2005. Growth of filter-feeding benthic invertebrates from a region with variable upwelling intensity. Mar. Ecol. Prog. Ser. 295, 79–89. http://dx.doi.org/10.3354/meps295079.

Reda, I., Andreas, A., 2008. Solar position algorithm for solar radiation applications (revised), Tech. Rep.. Golden, CO.

Rippy, M.A., Franks, P.J.S., Feddersen, F., Guza, R.T., Moore, D.F., 2013a. Factors controlling variability in nearshore fecal pollution: Fecal indicator bacteria as passive particles. Mar. Pollut. Bull. 66, 151–157. http://dx.doi.org/10.1016/j.marpolbul.2012.09.030.

Rippy, M.A., Franks, P.J.S., Feddersen, F., Guza, R.T., Moore, D.F., 2013b. Factors controlling variability in nearshore fecal pollution: The effects of mortality. Mar. Pollut. Bull. 66 (1–2), 191–198. http://dx.doi.org/10.1016/j.marpolbul.2012.09.003.

Ross, V., Dion, D., 2007. Sea surface slope statistics derived from sun glint radiance measurements and their apparent dependence on sensor elevation. J. Geophys. Res. 112, c09015. http://dx.doi.org/10.1029/2007JC004137.

Ruessink, B.G., Miles, J.R., Feddersen, F., Guza, R.T., Elgar, S., 2001. Modeling the alongshore current on barred beaches. J. Geophys. Res. 106, 22,451–22,463.

Ruessink, B., Walstra, D., Southgate, H., 2003. Calibration and verification of a parametric wave model on barred beaches. Coast. Eng. 48 (3), 139–149. http://dx.doi.org/10.1016/S0378-3839(03)00023-1.

Saunders, P.M., 1967. Shadowing on the ocean and the existence of the horizon. J. Geophys. Res. 72 (18), 4643–4649.

Sinnett, G.H., Feddersen, F., 2014. The surf zone heat budget: The effect of wave heating. Geophys. Res. Lett. 41, http://dx.doi.org/10.1002/2014GL061398.

Sinton, L., Davies-Colley, R., Bell, R.G., 1994. Inactivation of enterococci and fecal coliforms from sewage and meatworks effluents in seawater chambers. Appl. Environ. Microbiol. 60 (6), 2040–2048.

Sinton, L., Hall, C., Lynch, P., Davies-Colley, R., 2002. Sunlight inactivation of fecal indicator bacteria and bacteriophages from waste stabilization pond effluent in fresh and saline waters. Appl. Environ. Microbiol. 68 (3), 1122–1131.

Stockdon, H.F., Holman, R.A., 2000. Estimation of wave phase speed and nearshore bathymetry from video imagery. J. Geophys. Res. Oceans 105 (C9), 22,015–22,033. http://dx.doi.org/10.1029/1999JC000124.

Taylor, J., Edwards, J., Glew, M., Hignett, P., Slingo, A., 1996. Studies withi a flexible new radiation code. ii: Comparisons with aircraft short-wave observations. Q. J. R. Meteorol. Soc. 122, 839–861.
Thornton, E.B., Guza, R.T., 1983. Transformation of wave height distribution. J. Geophys. Res. 88 (C10), 5925–5938.
Walstra, D., Mocke, G.P., Smit, F., 1996. Roller contributions as inferred from inverse modelling techniques. In: Proceedings 25th International Coastal Engineering Conference, pp. 1205–1218.
Whitlock, C.H., Bartlett, D.S., Gurganus, E.A., 1982. Sea foam reflectance and influence on optimum wavelength for remote sensing of ocean aerosols. Geophys. Res. Lett. 9 (6), 719–722. http://dx.doi.org/10.1029/GL009i006p00719.